# Electron energy distributions and anomalous skin depth effects in high-plasma-density inductively coupled discharges

Alex V. Vasenkov* and Mark J. Kushner†

*Department of Electrical and Computer Engineering, University of Illinois, 1406 West Green Street, Urbana, Illinois 61801*

(Received 19 July 2002; published 19 December 2002)

Electron transport in low pressure (<10s mTorr), moderate frequency (<10s MHz) inductively coupled plasmas (ICPs) displays a variety of nonequilibrium characteristics due to their operation in a regime where the mean free paths of electrons are significant fractions of the cell dimensions and the skin depth is anomalous. Proper analysis of transport for these conditions requires a kinetic approach to resolve the dynamics of the electron energy distribution (EED) and its non-Maxwellian character. To facilitate such an investigation, a method was developed for modeling electron-electron collisions in a Monte Carlo simulation and the method was incorporated into a two-dimensional plasma equipment model. Electron temperatures, electron densities, and EEDs obtained using the model were compared with measurements for ICPs sustained in argon. It was found that EEDs were significantly depleted at low energies in regimes dominated by noncollisional heating, typically within the classical electromagnetic skin depth. Regions of positive and negative power deposition were observed for conditions where the absorption of the electric field was both monotonic and nonmonotonic.

DOI: 10.1103/PhysRevE.66.066411 PACS number(s): 52.27.−h, 52.80.Pi, 52.20.Fs, 52.50.Qt

## I. INTRODUCTION

The trend towards using high plasma density ($>10^{11}$ cm$^{-3}$), low gas pressure (<10s mTorr) sources in material processing has resulted in renewed interest in electron transport in inductively coupled plasma (ICP) discharges. Although the partial ionization in these devices can be large (>0.001–0.01), the electron energy distribution (EED) is often non-Maxwellian as a result of the power being deposited in a nonuniform and nonlinear fashion [1–10]. As a consequence, a kinetic approach is required to properly resolve electron energy transport. One of the challenges faced in simulating kinetic transport in ICPs with moderate fractional ionization is resolving electron-electron ($e$-$e$) collisions that significantly influence the thermal motion of electrons.

At least three approaches have been used to resolve $e$-$e$ collisions for the conditions of interest. The first is to treat $e$-$e$ collisions on particle-particle basis, as in particle-in-cell simulations [11–14]. Although robust, these techniques are computationally expensive, particularly for high fractional ionizations. The second approach is to use nonstatistical methods or a direct solution of Boltzmann's equation, which explicitly includes $e$-$e$ collisions [15,16]. Although this approach is also robust, only a few terms are typically included in the expansion of the electron velocity distribution function, and so the method may have limited application. The third approach is to use an electron Monte Carlo simulation (EMCS) [17,18]. EMCS methods share the advantages of particle-particle techniques in not making any *a priori* assumptions regarding the electron velocity distribution. They differ from particle-in-cell methods in that the $e$-$e$ collisions are resolved on a particle-mesh basis. This approach is also computationally robust while introducing some approximation in the dynamics of the $e$-$e$ collisions. Its disadvantage is that it must be coupled with other computational modules to obtain the electric and magnetic fields that accelerate the electrons.

In this paper we describe a methodology for simulating $e$-$e$ collisions in EMCS using particle-mesh techniques. The EMCS was imbedded into a two-dimensional (2D) plasma equipment model that was then used to conduct a computational investigation of the effect of $e$-$e$ collisions on EEDs and of the electron kinetics in ICPs sustained in argon. The method was validated by comparisons to experiments. We found that $e$-$e$ collisions mitigate the propensity for cool electrons to pool at the maximum of the plasma potential when that location is outside the classical skin depth. We also found that the electric field can decay nonmonotonically, as observed experimentally [5,10], and that these conditions also usually result in regions of positive and negative power deposition by electrons. However, regions of both positive and negative power deposition were also observed when the electric field decayed monotonically, indicating that this effect is perhaps a more general consequence of an anomalous skin depth.

Brief descriptions of the algorithms for $e$-$e$ collisions, their implementation into the EMCS, and the incorporation of the EMCS in the plasma equipment model are in Sec. II. Comparisons between computed and experimental plasma properties for ICPs sustained in Ar are presented in Sec. III. Results from a parametric investigation of the anomalous skin effect and nonlocal power deposition in ICPs are discussed in Sec. IV. Concluding remarks are in Sec. V.

## II. DESCRIPTION OF THE MODEL

In this section we describe a method for modeling $e$-$e$ collisions in which Coulomb collisions are treated using a

*Permanent address: Institute of Thermophysics, Novosibirsk, 630090, Russia. Electronic address: vasenkov@uiuc.edu

†Electronic address: mjk@uiuc.edu

 

test particle approach, and so can be readily included in the EMCS of low-pressure and high-density plasma systems. In particular, this technique has been implemented in the EMCS of the two-dimensional hybrid plasma equipment model (HPEM). The HPEM and EMCS have previously been described in Ref. [18] and references therein, and so only brief outlines are given here.

The HPEM is a two-dimensional plasma equipment model that consists of an electromagnetic module (EMM), an electron energy transport module (EETM), and a fluid kinetics module (FKM). Electromagnetic fields and corresponding phases are calculated in the EMM. These fields are then used in the EETM to obtain electron impact source functions and transport coefficients using either an EMCS or by solving the electron energy equation. (In this work, the EMCS option was used in the EETM.) These parameters are transferred to the FKM where momentum, continuity, and energy equations are solved for all heavy particles. A drift diffusion formulation is used for electrons to enable an implicit solution of Poisson's equation for the electrostatic potential. The species densities and electrostatic fields produced in the FKM are transferred to the EMCS and the EMM. These modules are iterated until a converged solution is obtained.

To properly couple electron kinetics into solution of Maxwell's equation, the electron current that appears as a source of the electromagnetic field in the plasma must reflect the nonlocal character of the EEDs. Plasma dynamics are often coupled to the electromagnetic fields using a cold conductivity that is appropriate for a collision dominated plasma. Numerous works over recent years have shown that for the conditions of interest, using a cold conductivity may not fully capture the electron dynamics. For example, Turner [19], Godyak, Piejak, and Alexandrovich [20], and Vahedi *et al.* [21] have investigated, theoretically and experimentally, noncollisional heating and warm plasma effects in ICP reactors, observations that are partly explicable by an anomalous skin effect.

To address these conditions we have improved upon the method first discussed in Ref. [22] to couple electron kinetics into the solution of Maxwell's equations, which captures much of this behavior. The method and recent improvements will be briefly described. The electric field is provided by a frequency domain representation of Maxwell's equation,

$$\nabla^2\vec{E}+\left(\frac{\omega}{c}\right)^2\vec{E}=i\omega\mu_0\vec{J}, \tag{1}$$

where $\vec{J}$, $\omega$, $c$, and $\mu_0$ are, respectively, the current density, frequency, speed of light, and vacuum permeability. In the frequency domain, all wave quantities are assumed to vary harmonically in time as $e^{i\omega t}$. The current density $\vec{J}$ contains contributions from the external antenna and currents that are generated in the plasma due to the electromagnetic wave. If using a cold plasma approximation, the electron current density $\vec{J}_e$ is

$$\vec{J}_e(\vec{r},t)=\sigma(\vec{r},t)\vec{E}(\vec{r},t), \tag{2}$$

where

$$\sigma(\vec{r})=\frac{q^2 n_e(\vec{r})}{m_e[\nu_m(\vec{r})+i\omega]}, \tag{3}$$

and $\sigma$, $q$, $m_e$, $n_e$, and $\nu_m$ are, respectively, conductivity, magnitude of electron charge, electron mass, electron density, and electron momentum transfer collision frequency. One typically ignores ion current due to the low mobility of ions. When warm plasma effects are important, the local contributions to plasma current due to electron acceleration by the electromagnetic wave at remote locations must be taken into account. This can be accomplished by replacing Eq. (2) with

$$\vec{J}_e(\vec{r},t)=\int\int\sigma(\vec{r},\vec{r}',t,t')\vec{E}(\vec{r}',t')d\vec{r}'\,dt', \tag{4}$$

where the volume integral is over the entire plasma and the time integral is from all previous times to the present. $\sigma(\vec{r},\vec{r}',t,t')$ is a Green's function that relates contributions to the present, local electron current density from the electromagnetic wave at remote locations at previous times.

In this work, $\vec{J}_e(\vec{r},t)$ is directly obtained from the EMCS by numerically computing $\sigma(\vec{r},\vec{r}',t,t')\vec{E}(\vec{r}',t')$ by sampling the electron trajectories. In principle, this approach captures warm plasma effects by, for example, sampling electron trajectories after a free flight resulting from acceleration by electromagnetic fields at remote locations and prior times. In the EMCS, a distribution averaged azimuthal, harmonic velocity $\nu_e(\vec{r}_l,t)$, where $\vec{r}_l$ is a given spatial mesh point, is computed. This is accomplished by collecting statistics on the trajectories of electron pseudoparticles on every update of their position and speed,

$$V_e(\vec{r}_l)=\frac{\sum_j w_j v_j\exp(i\omega t_j)\sum_k \alpha_k\delta[(\vec{r}_{l+k}\pm\frac{1}{2}\Delta\vec{r}_{l+k})-\vec{r}_j]}{\sum_J w_J\sum_k \delta[(\vec{r}_{l+k}\pm\frac{1}{2}\Delta\vec{r}_{l+k})-\vec{r}_j]}, \tag{5}$$

where $V_e(\vec{r}_l)$ is the complex amplitude of the electron speed and $w_j$ is the weighting of an individual electron pseudoparticles having azimuthal velocity $v_j$ at time $t_j$. $w_j$ accounts for the number of electrons each pseudoparticle represents and the time step used in the current advance of the trajectory. The first sum is over all electron pseudoparticles $j$ and the second sum is over adjacent mesh points $k$ to account for particle averaging using finite-sized-particle techniques [14]. $\alpha_k$ is a spatial weighting that incorporates the finite-sized-particle coefficients. Contributions to $V_e(\vec{r}_l)$ are summed over 10–100 s of rf cycles. The harmonic, azimuthal electron velocity is then

$$\nu_e(\vec{r},t)=|V_e(\vec{r})|\cos(\omega t+\phi_l(\vec{r})),\quad \phi_l=\tan^{-1}\frac{\mathrm{Im}(V_e(\vec{r}))}{\mathrm{Re}(V_e(\vec{r}))}. \tag{6}$$

The electron current used in the EMM in the next iteration through the HPEM is then

$$J_e(\vec{r},t)=qn_e(\vec{r})v_e(\vec{r},t), \tag{7}$$

where $n_e(\vec{r})$ is the electron density obtained from the FKM. For computational stability, the electron current density used in the EMM is divided into two components,

$$\vec{J}_e(\vec{r},t)=\sigma(\vec{r})\vec{E}(\vec{r},t)+\vec{J}_{er}(\vec{r},t), \tag{8}$$

where $\vec{J}_{er}(\vec{r},t)=\vec{J}_e(\vec{r},t)-\sigma(\vec{r})\vec{E}(\vec{r},t)$, a residual current, is the difference between the warm current density computed in the EMCS and the cold plasma current. Since the kinetically derived electron current from the EMCS is held constant during the EMM, its direct use would not necessarily be computationally stable as it would represent a constant electron current independent of the local wave properties.

Electron transport properties and EEDs are obtained from the EMCS. The EMCS is a $3v$-$3D$ (three velocity components, three dimensions) model that integrates electron trajectories from electric and magnetic fields obtained using the EMM and FKM, and employs Monte Carlo techniques for collisions. At the beginning of the first call to the EMCS, electrons are initially given a Maxwellian velocity distribution and placed in the reactor using a distribution weighted by the local electron density obtained from the FKM. Pseudoparticle trajectories are advanced using the Lorentz equation,

$$\frac{d\vec{v}}{dt}=\frac{q_e}{m_e}(\vec{E}+\vec{v}\times\vec{B}), \quad \frac{d\vec{r}}{dt}=\vec{v}, \tag{9}$$

where $\vec{v}$, $\vec{E}$, and $\vec{B}$ are the electron velocity, local electric field, and magnetic field, respectively. The electric field contains rf contributions from the EMM and electrostatic contributions from the FKM. The electric field from the EMM, obtained from a frequency domain solution, is represented by its harmonic amplitude and phase as a function of position, and these quantities are interpolated to the particle's position based on the particle's phase during the rf cycle. The electrostatic field from the FKM is binned according to space and phase in the rf cycle. These electric fields are then interpolated in both space and phase. In this work, the magnetic field contains only harmonic rf contributions from the EMM as no magnetostatic field was imposed. The range of electron energies of interest is divided into discrete energy bins. Energy bins have constant widths over a specified energy range to simplify gathering statistical data while resolving structure in electron impact cross sections. A total of 300–500 bins are usually used with typical energy ranges (100 bins/range depending on the chemistry) of 0–5, 5–15, 15–50, and 50–200 eV.

Within energy bin $i$, the total collision frequency $v_i$ is computed by summing all the possible collisions with heavy particles,

$$v_i=\left(\frac{2\varepsilon_i}{m_e}\right)^{1/2}\sum_{j,k}\sigma_{ijk}N_j, \tag{10}$$

where $\varepsilon_i$ is the average energy within the bin, $\sigma_{ijk}$ is the cross section at energy $i$ (for species $j$ and collision process $k$), and $N_j$ is the number density of species $j$. As this juncture, $v_i$ does not account for the frequency of $e$-$e$ collisions owing that this frequency depends on the relative velocity of the collision partners and, therefore, depends on the dynamics of these trajectories during the simulation.

Null collision cross sections are employed for each energy range to provide a constant collision frequency. This is accomplished by adding an additional fictitious process referred to as a null collision such that all electrons appear to have the same collision frequency [23]. The null collisional frequency at energy $\varepsilon_i$ is $v_{ni}=v_m-v_i$, where $v_m$ is the maximum collision frequency based on both electron energy and density of collision partners. (In practice, separate maximum collision frequencies and null collision frequencies are used for subintervals of the energy distribution to minimize the occurrence of null collisions.) In doing so, the time between collisions can be obtained by $\Delta t=-\ln(r_1)/v_m$, where $r_1$ is a random number distributed on (0,1). The type of collisional event is determined by generating a series of random numbers. If $r_2\leqslant v_{ni}/v_m$, then the collision is null and the electron trajectory continues unhindered. For a real collision, we find the particular electron collision $j$ that satisfies

$$\frac{1}{v_m}\sum_{k=1}^{j-1}v_k<r_3\leqslant\frac{1}{v_m}\sum_{k=1}^{j}v_k, \tag{11}$$

where all collision frequencies are computed based on the maximum density of collision partner for process $j$, i.e., $N_{mj}$, in the entire reactor. A second level of null collision is then considered to determine whether the local density of the collision partner is large enough to warrant a collision. That is, if $r_4\leqslant N_j(\vec{r})/N_{mj}$, where $N_j(\vec{r})$ is the actual local density of the collision partner, then a real collision occurs. Otherwise, the collision is considered null.

The final velocity following a collision is determined by applying the scattering matrix,

$$\begin{aligned}V_x&=V(\cos\beta\cos\alpha\sin\theta\cos\phi+\cos\beta\sin\alpha\cos\theta\\&\quad-\sin\beta\sin\theta\sin\varphi),\\V_y&=V(\sin\beta\cos\alpha\sin\theta\cos\phi+\sin\beta\sin\alpha\cos\theta\\&\quad+\cos\beta\sin\theta\sin\varphi),\\V_z&=V(-\sin\alpha\sin\theta\cos\phi+\cos\alpha\cos\theta),\end{aligned} \tag{12}$$

where $\alpha$ and $\beta$ are the polar and azimuthal Eulerian angles of the electron velocity prior to the collision; $\theta$ and $\phi$ are the polar and azimuthal scattering angles, and $V$ is the electron speed after the collision. Assuming azimuthal symmetry for the collision, $\phi$ is randomly chosen from the interval $(0,2\pi)$. Unless experimental data are available, $\theta$ is chosen by specifying a scattering parameter $\gamma$ where the polar scattering probability is given by $\cos^{\gamma}(\theta/2)$. $\gamma=0$ provides for isotropic scattering and $\gamma\gg1$ provides for forward scattering. The randomly selected scattering angle is then

$$\theta=2[\cos^{-1}(1-r)]^{[1/(2+\gamma)]}, \tag{13}$$

where $r$ is a random number distributed (0,1).

Statistics are collected for every particle on every time step. The particles are binned by energy and location with a weighting proportional to the product of the number of electrons each pseudoparticle represents and its last time step. Particle trajectories are integrated for ≈100 rf cycles for each call of the EETM. Statistics are typically gathered for only the latter two-thirds of those cycles to allow transients that occur at the beginning of each iteration to dampen out. The time step for advancement is the shortest of the time to the next collision, the time required to cross a specified fraction of the local computational cell (typically 0.25) or a specified fraction of the rf cycle (typically 0.01). Since the time step is different for each pseudoparticle, they diverge in time, a process that continues until the pseudoparticles reach a specified future time. At that time, a pseudoparticle is no longer advanced until all other particles catch up.

At the end of a given iteration, the EED at each spatial location is obtained by normalizing the statistics such that

$$\sum_i F_i(\vec{r}) = \sum_i f_i(\vec{r}) \varepsilon_i^{1/2} \Delta\varepsilon_i = 1, \tag{14}$$

where $F_i(\vec{r})$ is the sum of the pseudoparticles' weightings at $\vec{r}$ for energy bin $i$ having energy $\varepsilon_i$, $f_i(\vec{r})$ ($\mathrm{eV}^{-3/2}$) is the EED at $\vec{r}$, and $\Delta\varepsilon_i$ is the width of the energy bin.

We have found that, for a given computational investment, it is more desirable to integrate the trajectories of a smaller number of pseudoparticles for a larger number of cycles, than a larger number of particles for a smaller number of cycles. The average number of particles (accounting for ionization and losses) is about $10^4$, and so there are approximately $10^8$ samplings per call of the EMCS. A typical 2D mesh has $50\times50$ points, resulting in $10^4-10^5$ sampling per mesh point. Based on this sampling the accuracy of calculated EEDs in the energy range below 15 eV is estimated to be a few percent near the position of maximum of electron density.

The goal of our method is to treat $e$-$e$ collisions using a test particle approach. That is, instead of electrons colliding with each other, as in particle-particle methods [11–14], the electrons collide with an energy resolved electron fluid. Essentially, our algorithm addresses $e$-$e$ collisions on a particle-mesh basis [17]. This is accomplished by using spatially dependent EEDs recorded during previous iterations.

Accounting for $e$-$e$ collisions for pseudoelectron particles is performed on every time step in the following manner. The incident pseudoelectron begins with velocity $\vec{v}_0$. The velocity of an electron collision partner for the incident pseudoelectron is randomly chosen from the local EEDs that were computed on the previous iteration. As only the EED, as opposed to the electron velocity distribution, is retained from the previous iteration, we assume that the chosen target electron has an isotropic angular distribution. In doing so, the probability of having a collision partner with an energy $\varepsilon'$ for a pseudoelectron in the $j$th spatial bin in time interval $\Delta t$ is determined with a cumulative probability

$$P_j(\varepsilon') = f_j(\varepsilon') \varepsilon'^{1/2} \Delta\varepsilon' \Big/ \left( \sum_j f_j(\varepsilon_i') \varepsilon_i'^{1/2} \Delta\varepsilon' \right), \tag{15}$$

where $f_j(\varepsilon')$ is the EED in the $j$th bin and the summation is over the entire energy range. The energy of the target electron, $\varepsilon_i'$, is that which satisfies

$$\Pi_j(\varepsilon_{i-1}') < r \leqslant \Pi_j(\varepsilon_i'), \tag{16}$$

where $r$ is a random number distributed (0,1). The cumulative probability $\Pi_j(\varepsilon_i')$ in the $j$th spatial bin is determined from

$$\Pi_j(\varepsilon_i') = \sum_{k=1}^{i} P_j(\varepsilon_k') \Big/ \sum_k P_j(\varepsilon_k'), \tag{17}$$

where the summation in the denominator is over subenergies, so that $\Sigma_i \Pi_j(\varepsilon_i') = 1$.

These probabilities are precomputed at the beginning of each iteration. Since the number of energy bins on which $P_j(\varepsilon')$ is stored is usually large (400–500), we implemented a quick lookup technique for $\varepsilon'$. The energy interval of interest is divided into smaller number of energy ranges centered at $E_l$ (typically 10–12) containing many of the fundamental energy bins $\Delta\varepsilon_i$. The size of $l$th range, $\Delta E_l$, is chosen so that the function

$$\Xi_{jl} = \sum_{E_l - \Delta E_l/2 \leqslant \varepsilon' < E_l + \Delta E_l/2} \Pi_j(\varepsilon')$$

has the same value for any $l$. The energy of the collision partner, $\varepsilon'$, is first randomly selected on a coarse basis using the functions $\Xi_{jl}$, followed by a refinement within the large energy intervals using cumulative probability $\Pi_j(\varepsilon')$. This two-stage lookup significantly reduces the computational time for simulating $e$-$e$ collisions.

Once the velocity of partner, $\vec{v}'$, is chosen, the impact parameter for a 90° scattering, $b_0$, is determined [24,25] as

$$b_0 = e^2/(2\pi\varepsilon_0 m_e g^2), \tag{18}$$

where $m_e$ is the mass of electron, $g = |\vec{v}_0 - \vec{v}'|$ is the relative speed of the collision partners, and $\varepsilon_0$ is the vacuum permittivity. If $\cos(\theta) < b_0/\lambda_D$, where $\theta$ is the angle between velocity of the pseudoelectron and its collision partner and $\lambda_D$ is the local Debye length, the collision event is ignored. Although scattering through very small angles may not be well represented by this approach, such scattering does not appreciably affect the EED at energies that determine inelastic rate coefficients. As a result, our predicted discharge properties were not appreciably affected. The logic to this step is that we assume that the changes in charge densities, which may occur on spatial scales larger than $\lambda_D$, do not contribute to Coulomb collisions between electrons. Otherwise, the probability of an $e$-$e$ collision during the current time step $\Delta t$ is determined from

$$P_{e\text{-}e}(g, \Delta t) = n_j \sigma_{e\text{-}e}(g) g \Delta t, \tag{19}$$

where $n_j$ is the density of electrons in the $j$th spatial bin obtained from the FKM, and the momentum transfer Coulomb cross section $\sigma_{e\text{-}e}(g)$ (Ref. [21]) is

$$\sigma_{e\text{-}e}(g)=4\pi b_0^2[1+\ln(\lambda_d/b_0)^2]^{1/2}. \tag{20}$$

This process is justified if, for the conditions of interest, $P_{e\text{-}e}(g,\Delta t)\ll 1$, which is the case for virtually all conditions of this study. The collision event takes place if $P_{e\text{-}e}(g,\Delta t)\geqslant r$. If a collision occurs, then a postcollision relative velocity $\vec{g}'$ is randomly determined [26] such that

$$g_z'=\pm|\vec{g}|r_1, \quad g_x'=|\vec{g}|\sqrt{1-r_1^2}\cos(2\pi r_2),$$

$$g_y'=|\vec{g}|\sqrt{1-r_1^2}\sin(2\pi r_2), \tag{21}$$

where $r_1$ and $r_2$ are two independent random numbers, and $g_z'$ is positive or negative if $g_z$ is positive or negative, respectively. Finally, the final velocity of the pseudoelectron, $\vec{v}_f$, is updated with

$$\vec{v}_f=\vec{v}_R+0.5\vec{g}', \quad \vec{v}_R=0.5(\vec{v}'+\vec{v}_0), \tag{22}$$

The change in the velocity of collision partner in the mesh-stored distribution function is disregarded. In doing so, $e$-$e$ collisions are treated as collisions between pseudoelectrons and energy resolved electron fluid, whose properties will reflect the consequences of the $e$-$e$ collision during the next update of the binned EEDs. The cumulative effects of successive binary $e$-$e$ scattering, both small and large angles, are captured by the collection of statistics on the spatially dependent EEDs during the current iteration, which are then used for collisional integrals on the subsequent iteration. A single pseudoparticle is sampled roughly $10^4$ times per iteration (100 samplings per rf cycle for 100 rf cycles per iteration) and the model iterates through the HPEM modules roughly 50–100 times per case. These sampling rates should provide sufficient opportunity for self-consistency between the real-time EEDs and those used in the collision integrals.

Power deposition from the inductive electric field by electrons is directly computed in the EMCS as the ensemble time average (over many rf cycles) of the product of the electron velocity and local electric field,

$$P(\vec{r})=\frac{n_e(\vec{r})\sum_j w_j q_j(\vec{v}\cdot\vec{E})\,\delta(\vec{r}-\vec{r}_j)}{\sum_j w_j\,\delta(\vec{r}-\vec{r}_j)}, \tag{23}$$

where the sum is over pseudoparticles. Positive power deposition represents net transfer from the electric field to the electrons. Negative power deposition represents a net transfer of power from the electrons to the electric field.

## III. PLASMA PROPERTIES AND ELECTRON ENERGY DISTRIBUTIONS

In this section we present the results of our investigations of EEDs in an ICP reactor. The model was validated using experimental data from the literature [27,28]. A schematic of the reactor used in our study is shown in Fig. 1. The chamber is cylindrically symmetric, 10 cm in radius and 10.75 cm tall. The antenna is a five-turn coil set atop a quartz window 1.27 cm thick. A Faraday shield greatly reduces capacitive coupling, which we have ignored in the model. Argon is injected below the window and pumped at the bottom of the reactor. In our computations, continuity, momentum, and energy equations are solved for all heavy particles (ions and neutrals). A drift-diffusion formalism is used for electron densities coupled with a semi-empirical solution for the Poisson equation. The reaction mechanism for the Ar plasma used here is given in Table I.

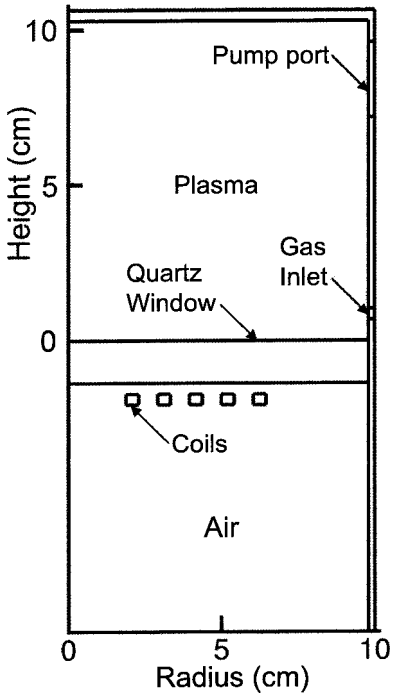


FIG. 1. Schematic of the ICP reactor.

Plasma densities, densities of Ar($4s$) and electron impact ionization source function are shown in Fig. 2 for the base case conditions of 10 mTorr, 100 W, and 6.78 MHz. Electron temperature and effective ion temperature, which account for both random and directed energies, are shown in Fig. 3. The plasma density is rather uniform over the radius at the top and bottom boundaries. The maximum of plasma density occurs in the middle of reactor where the electric potential is maximum and at the edge of the classical skin depth ($\delta\approx 2$ cm) where the amplitude of the electromagnetic field decays to $1/e$ of its edge value. The electron temperature has a peak in the electromagnetic skin depth resulting from collisionless heating by the large electric field. The electron temperature varies by less than an eV across the reactor, a consequence of both the long mean free path of electrons accelerated in the skin depth enabling those electrons to retain their energy across the reactor and, in an opposite sense, the large $e$-$e$ collision frequency that redistributes energy through the electron thermal conductivity. In contrast, the effective ion temperature is maximum when close to the walls, where ions gain energy from acceleration in the

TABLE I. Reaction mechanism.

| Species: Ar($3s$), Ar*($4s$), Ar**($4p$), $e$ | | |
|---|---|---|
| Reaction | Rate coefficient[a] | Reference |
| $e+\mathrm{Ar}\rightarrow\mathrm{Ar}+e$ | [b] | [29] |
| $e+\mathrm{Ar}\rightarrow\mathrm{Ar}^*+e$ | [b] | [30] |
| $e+\mathrm{Ar}\rightarrow\mathrm{Ar}^{**}+e$ | [b] | [30] |
| $e+\mathrm{Ar}\rightarrow\mathrm{Ar}^+ +e+e$ | [b] | [31] |
| $e+\mathrm{Ar}^*\rightarrow\mathrm{Ar}^+ +e+e$ | [b] | [32] |
| $e+\mathrm{Ar}^*\rightarrow\mathrm{Ar}+e$ | [b] | [30] |
| $e+\mathrm{Ar}^*\rightarrow\mathrm{Ar}^{**}+e$ | [b] | [33] |
| $e+\mathrm{Ar}^{**}\rightarrow\mathrm{Ar}+e$ | [b] | [30] |
| $e+\mathrm{Ar}^{**}\rightarrow\mathrm{Ar}^+ +e+e$ | [b] | [34] |
| $e+\mathrm{Ar}^{**}\rightarrow\mathrm{Ar}^*+e$ | [b] | [33] |
| $\mathrm{Ar}^*+\mathrm{Ar}^*\rightarrow\mathrm{Ar}^+ +\mathrm{Ar}+e$ | $1\times10^{-9}$ | [35] |
| $\mathrm{Ar}^{**}+\mathrm{Ar}^{**}\rightarrow\mathrm{Ar}^+ +\mathrm{Ar}+e$ | $1\times10^{-9}$ | [35] |
| $\mathrm{Ar}^{**}+\mathrm{Ar}^*\rightarrow\mathrm{Ar}^+ +\mathrm{Ar}+e$ | $1\times10^{-9}$ | [35] |
| $\mathrm{Ar}^{**}\rightarrow\mathrm{Ar}^*$ | $1\times10^5$ s$^{-1}$ | [c] |
| $\mathrm{Ar}^+ +\mathrm{Ar}\rightarrow\mathrm{Ar}^+ +\mathrm{Ar}$ | $5.66\times10^{-10}$ | [36] |

[a]Rate coefficients have units of cm$^3$/s unless noted otherwise.
[b]Rate coefficient is calculated from electron energy distribution obtained in the EMCS using the cross section from the cited reference.
[c]Estimated for a mildly trapped optical transition.

presheath. In the middle of reactor, the effective ion temperature is lower due to thermalizing collisions with neutral species.

The density of Ar($4s$) differs from plasma densities as this state is only created by electrons with energies higher than 11.6 eV, either directly by collision with the ground state or indirectly by excitation to Ar($4p$), followed by radiative relaxation or quenching to Ar($4s$). The state is dominantly quenched by electrons having lower energy by superelastic collisions or electrons with energy greater that 3.5 eV by ionization. The sources for Ar($4s$) are therefore dominantly in the lower part of the reactor where the tail of the distribution is more extended whereas the sinks for this state are distributed throughout the reactor. Conversely, ionization for these conditions is dominated by multistep processes out of Ar($4s$) and Ar($4p$), having an effective ionization potential of 3.5 eV, whereas volumetric sinks for the ions are negligible. Therefore, net ionization sources are more widely distributed than for Ar($4s$), producing a peak in the center of the reactor.

Computed electron densities and temperatures are compared with experiments [27] (as shown in Fig. 4) for the base case conditions at $r=0$ cm. The electron density profile agrees well with the measurements. The maximum of electron density occurs at about $z=4$ cm, displaced from the center due to the lower axial location of the peak of the electron source function. The high thermal conductivity and redistribution of energy resulting from $e$-$e$ collisions produce nearly uniform electron temperatures with a maximum occurring near the quartz window where power deposition is largest. The calculated electron temperature is 0.5 eV below that of measurements, but reproduces well the shape of the measured temperature profile.

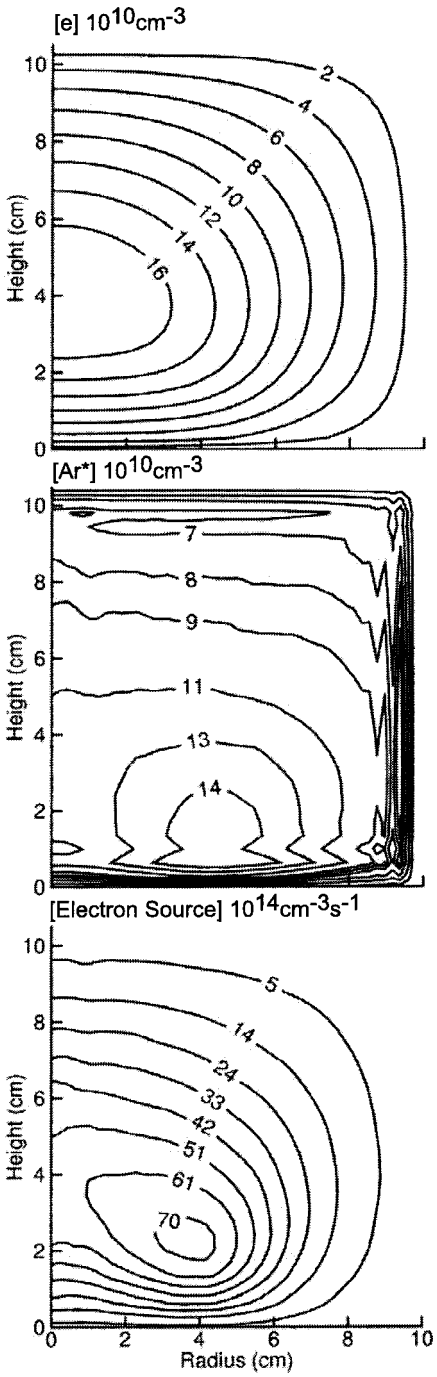


FIG. 2. Plasma parameters for the base case conditions (10 mTorr, 100 W, 6.78 MHz). (a) Plasma density, (b) Ar($4s$) density, and (c) electron impact ionization source function. Plasma densities are maximum near the peak in the plasma potential while Ar($4s$), having larger bulk quenching collisions, peaks near the coils where the electron temperature is higher.

The consequences of $e$-$e$ collisions on the EEDs are shown in Fig. 5 for 10 mTorr, 200 W, and 6.78 MHz. EEDs at the position of maximum plasma density and plasma potential ($r=1$ cm and $z=3$ cm) are shown in Fig. 5(a). EEDs at $(r,z)=(4,3\,\mathrm{cm})$, for both a lower electron density and plasma potential, are shown in Fig. 5(b). The EED without $e$-$e$ collisions at the maximum in electron density and

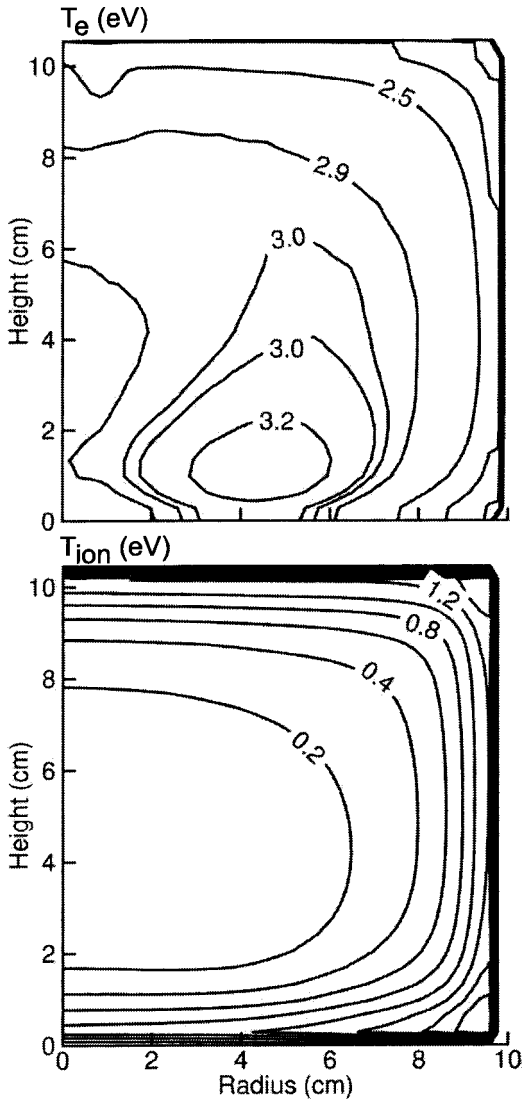


FIG. 3. Plasma parameters for the base case conditions (10 mTorr, 100 W, 6.78 MHz). (a) Electron temperature and (b) effective ion temperature, which is a sum of random and directed energies. The electron temperature peaks in the classical skin depth. The effective ion temperatures are maximum in the presheath, where the ambipolar fields are larger.

plasma potential rapidly increases in magnitude as the energy approaches zero. This trend is due to the propensity for low-energy electrons to ''pool'' at the peak in plasma potential which, for our conditions, is beyond the classical skin depth. Low-energy electrons near the peak in plasma potential do not have sufficient energy to climb the potential gradient back into classical skin depth where they can be heated; and so, in the absence of superelastic collisions, have no mechanism to increase their energy. When including *e-e* collisions, the fraction of low-energy electrons at the peak of the plasma potential is smaller owing to the energy transfer between low-energy and high-energy electrons; that is, there is a mechanism to heat low-energy electrons, which allows them to escape from the potential well. The *e-e* collisions are the mechanism providing for thermal conductivity. In the absence of *e-e* collisions, the electron temperature, in fact, has

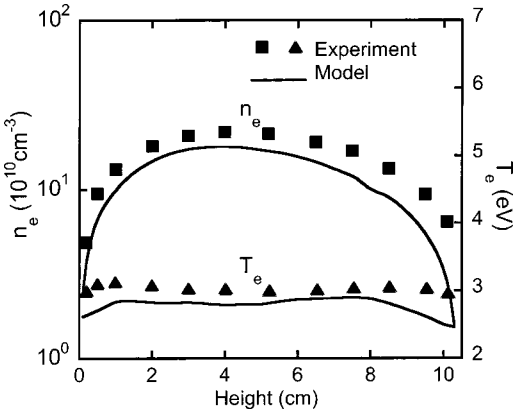


FIG. 4. Comparison of calculated axial spatial profiles (at $r=0$ cm) of electron density and electron temperature with measurements (Ref. [27]) for the base case (10 mTorr, 100 W, 6.78 MHz).

a significant minimum in the center of the plasma resulting from this pooling effect. The EEDs at $(r,z)=(4,3$ cm) have less dramatic differences between including and excluding *e-e* collisions, though the low-energy pooling is still evident. The plasma potential is less positive at this location resulting in less propensity to pool there, and the electron density is smaller resulting in fewer *e-e* collisions to redistribute the electron energy.

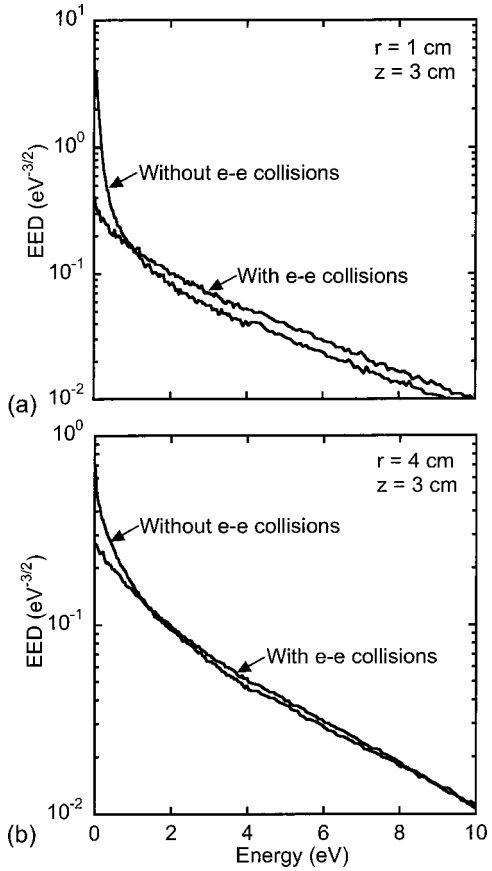


FIG. 5. EEDs when including and excluding *e-e* collisions at $z=3$ cm. (a) $r=1$ cm, (b) $r=-4$ cm. (6.78 MHz, 10 mTorr, 200 W). In the absence of *e-e* collisions, cool electrons pool near the peak in the plasma potential.

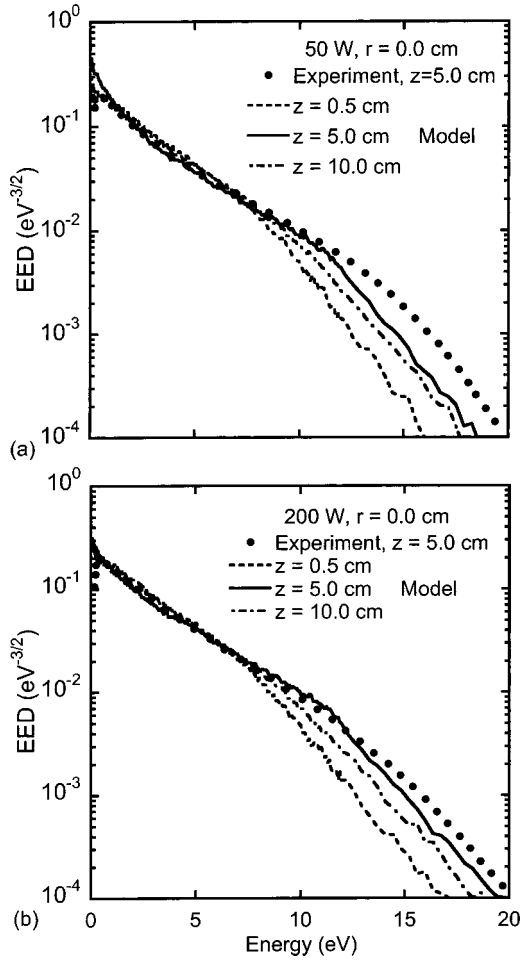


FIG. 6. Comparison of calculated EEDs with experiments (Ref. [28]) at $r=0$ cm, 6.78 MHz, and 10 mTorr. (a) 50 W and (c) 200 W. Calculated EEDs are shown at different heights, lower heights being closer to the coils. Lower power producing a smaller electron density and having fewer $e$-$e$ collisions has a larger thermal component of the EED.

Comparisons between computed and measured [28] EEDs in the center of the reactor are shown in Fig. 6 for powers of 50 and 200 W. Computed EEDs are compared to experiments in the classical skin layer (0.5 cm), at midheight (5 cm), and near the wall opposite the coils (10 cm). The normalization for both numerical and experimental results is to have the integral over the electron distribution equal to 1. In doing so, the experimental data are approximated by straight lines at very low energies. The computed EEDs, in general, agree well with those obtained from experiments. The differences at very low energies are attributed in part to rf probe distortion and in part to our algorithm. At 50 W, the computed and experimental EEDs have positive curvature for energies less than 10 eV, indicating a tendency towards thermalization and energy pooling in the center of the reactor beyond the classical skin depth. The EEDs in the classical skin layer and near the top wall have a bi-Maxwellian shape, which is typical for low-pressure inductively coupled plasmas and which do not have significant energy pooling [37,38]. Owing to the azimuthal electric field being small in the vicinity of the axis, the tail of the EED near the coils ($z=0.5$ cm) is lower than in the center of the plasma. This is a consequence of the electron density being smaller on axis near the walls, thereby limiting thermal conduction (through $e$-$e$ collisions) from more energetic electrons at larger radii. Electrons accelerated in the skin layer where the electric field is largest ($r\approx 5$ cm) are also unlikely to convect towards the axis, thereby inhibiting heating of the tail.

Near the center of the reactor, electron thermal conduction through $e$-$e$ collisions from the skin layer is more rapid and convection of electrons from the skin layer is more probable. Both effects produce an increase in the tail of the EED. The calculated EED at the center of the reactor is best represented by a three-temperature Maxwellian distribution, a distribution often used to characterize EEDs in low-pressure ICPs (Ref. [39]). The distribution has a low temperature for energies about the Ramsauer minimum and where pooling occurs, a higher temperature in the medium energy range below the first threshold of inelastic collisions, and again a lower temperature at energies above the first threshold of inelastic collisions. At 200 W the trends are similar, however, electron thermalization produced by Coulomb collisions causes the EED in the center of the reactor to approach a Maxwellian, thereby reducing the energy pooling effect. The agreement with experiment is less good at 50 than at 200 W, as the tail of the EED is underpredicted at the lower power. This could be a result of an offset in the spatial distribution of the computed EEDs compared to the experiment or an inaccuracy in the predicted sheath structure, which allows an inordinate number of higher-energy electrons to escape. The loss of ionization by the loss of these higher-energy electrons could also explain why the predicted electron densities are less than the experiment as well.

The EEDs at $r=0$ (Fig. 6) are only indirectly affected by collisionless heating in the skin layer since the azimuthal electric field is zero on axis. The EEDs at $r=4.5$ cm near the radial peak of the electric field, shown in Fig. 7 for various heights, are more strongly affected by collisionless heating in the skin layer. The general trend is that there is a monotonic decrease in the tail of the EED from the skin layer across the reactor to the opposite wall. These electrons, having energies generally greater than 10 eV, are less affected by $e$-$e$ collisions whose cross section scales as $1/\varepsilon^2$. The damping of the tail is largely a consequence of inelastic collisions. The EED at $z=0.4$ cm is rather depleted at low energies while the tail of the EED is highest, indicating that large numbers of electrons are accelerated out of the skin layer by the electric field. This in turn requires that the electron mean free path is commensurate to the depth of the skin layer; that is, the skin layer is anomalous. This EED can be well represented by a bi-Maxwellian distribution with temperatures of 4.1 eV (low energy) and 2.3 eV (tail).

The EED at $z=1.7$ cm is less depleted at low energies as the acceleration is smaller being deeper into the skin layer, and so the effective temperature of the electrons is only 3.5 eV. For the base case conditions, the axial force on electrons due to Lorentz acceleration by the rf magnetic field is approximately equal to that by the azimuthal electric field [7]. The tail of EED at $z=1.7$ has nearly the same slope as the

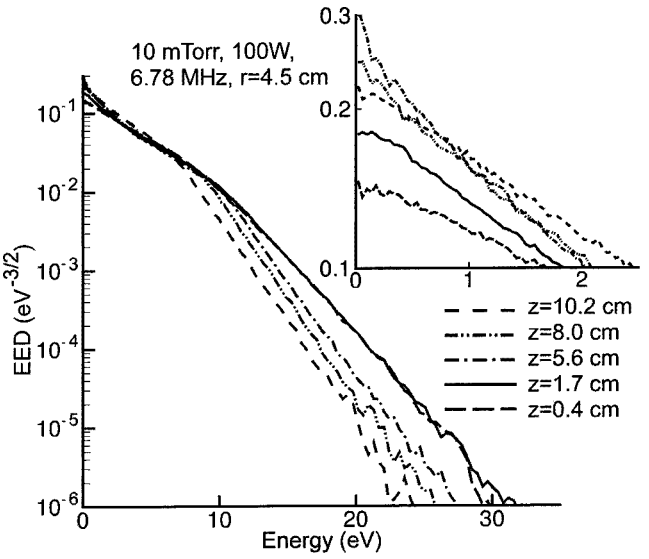


FIG. 7. EEDs at $r=4.5$ cm and different heights for 6.78 MHz, 100 W, and 10 mTorr. The inset shows the EEDs at low energies. EEDs near the peak of the plasma potential have a larger thermal peak due to pooling of low-energy electrons. The tail of the EED is extended in the skin depth.

EED at $z=0.4$ cm as a consequence of this axial acceleration and the mean free path of the electrons being commensurate to the differences in height. The EED in the center of the reactor ($z=5.6$ cm) displays the three-temperature features described earlier due to the influence of $e$-$e$ collisions. This EED is enhanced at very low energies due to the Ramsauer minimum in the momentum transfer cross section and pooling of low-energy electrons. The effective temperature for electrons in this energy range is $\approx$2.1 eV. The electron temperature is higher (3.8 eV) at moderate energies, and is lower (1.8 eV) for the tail of EED. The EED at $z=8.0$ cm is slightly depleted at low energies due to pooling of electrons from this region towards the peak of the plasma potential. The temperatures for this tri-Maxwellian EED are 2.9, 3.3, and 1.7 eV. The EED at $z=10.2$ cm can again be approximated by a bi-Maxwellian distribution with temperatures 3.1 and 1.7 eV.

The consequences of gas pressure on electron transport are shown in Fig. 8 where EEDs are given for 1, 10, and 30 mTorr at $r=0$ and $z=0.5$, 5, and 10 cm. The EEDs vary due to the transition from a regime of nearly total collisionless electron heating at 1 mTorr to a regime of collisional heating at 30 mTorr. In the case of 1 mTorr, the structure of the EEDs is dominated by collisionless heating and by nonlinear Lorentz forces that provide an axial acceleration. These processes most significantly affect the EED in the skin layer. At energies below the first threshold of inelastic collisions, this EED can be represented by a single Maxwellian distribution with a rather high temperature of 13 eV. Electrons with energies above the thresholds for inelastic events more efficiently transfer power to the gas, and consequently, the effective temperature for these electrons in the tail of the EED is lower, about 6 eV. The EED at $z=5$ cm is affected by stochastic heating, collisions, and pooling as the peak in the

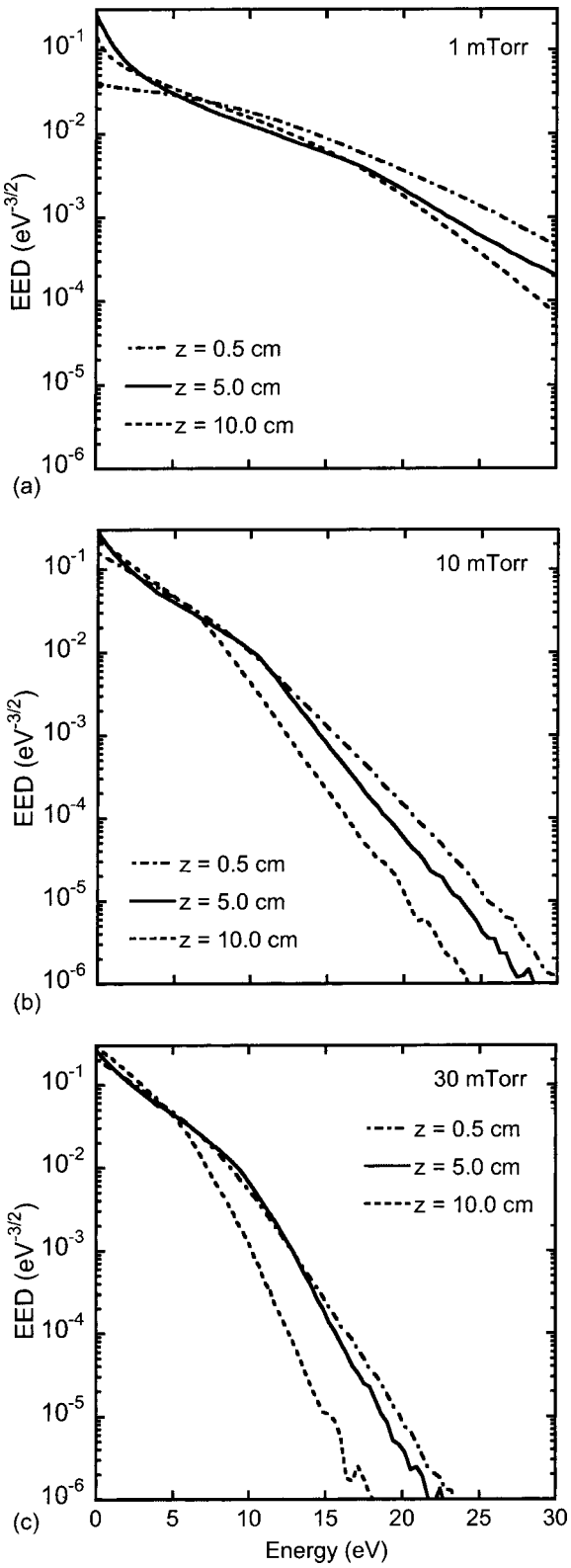


FIG. 8. Consequences of gas pressure on EEDs at 100 W, 6.78 MHz, and $r=4.5$ cm. (a) 1 mTorr, (b) 10 mTorr, and (c) 30 mTorr. EEDs are shown in the skin layer ($z=0.5$ cm), in the middle of the reactor (5 cm) and near the opposite wall (10 cm). Electron heating transition from collisionless at 1 mTorr to collisional at 30 mTorr.

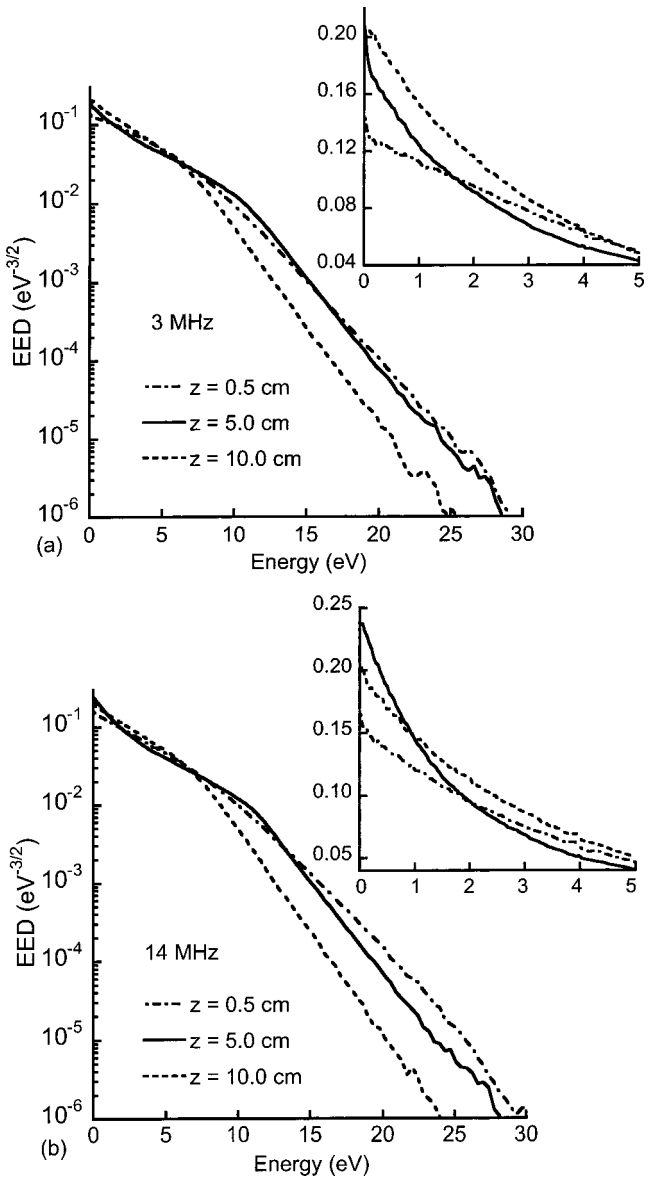


FIG. 9. EEDs for (a) 3 MHz and (b) 14 MHz at 100 W, 10 mTorr, $r=4.5$ cm at different heights in the reactor. The inset shows EEDs at low energies. The longer skin depth and larger Lorentz forces at the lower frequency raises the tail of the EED in the middle of the reactor.

plasma potential at 1 mTorr is larger. This EED is best represented by a three-temperature Maxwellian distribution: $T_1=1.4$ eV for lower energies near the Ramsauer minimum extending to a few eV, a higher temperature $T_2=6.2$ eV for energies from 5 to 18 eV, and a lower temperature $T_3=4.1$ eV for higher energies. The EED near the wall opposite to the coils (10 cm) is less affected by collisionless heating and pooling. This EED can also be represented by a three-temperature distribution: $T_1=2.6$ eV for energies near the Ramsauer minimum (larger than in the center of the reactor due to less pooling there), $T_2=6.1$ eV for energies from 2 to 15 eV and $T_3=3.3$ eV for higher energies (also smaller than in the center of the reactor indicative of being beyond the range of electrons heated in the skin layer).

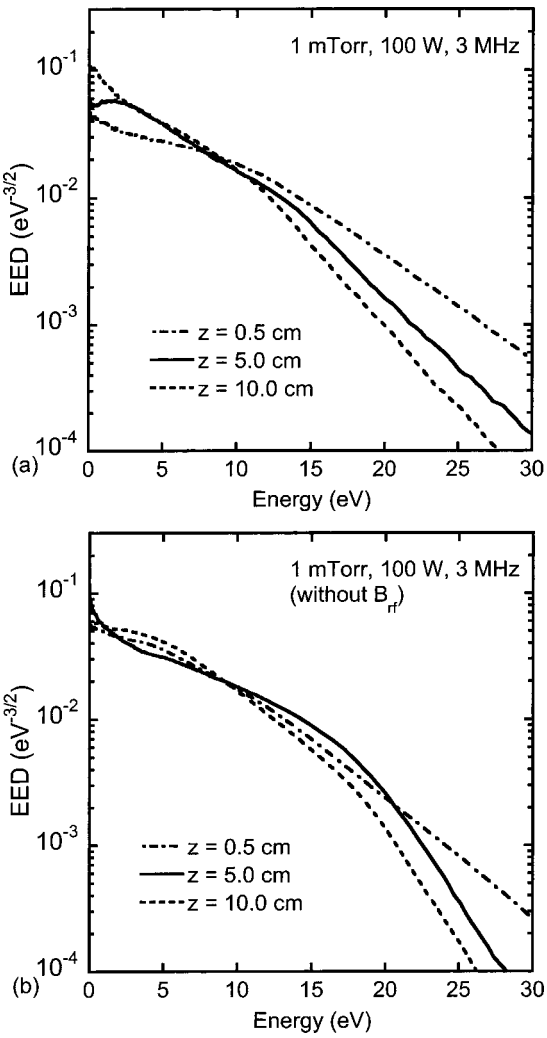


FIG. 10. EEDs obtained when (a) including and (b) excluding Lorentz acceleration due to the rf magnetic field for 1 mTorr, 100 W, and 3 MHz at $r=4.5$ cm. When the skin layer is anomalous, the EED is significantly affected by Lorentz forces.

At 10 mTorr, stochastic heating is of less importance. In the skin layer the EED can be again represented by a bi-Maxwellian distribution with two temperatures: 3.7 and 2.3 eV. These temperature are considerably lower than those in the skin layer at 1 mTorr due to the higher collisionality at this pressure. EEDs at $z=5$ and 10 cm are well represented by three-temperature distributions owing to electrons not experiencing significant collisionless heating. Electron heating at 30 mTorr is dominated by collisional processes, and so the EEDs resemble Druyvesteyn distributions.

The EEDs obtained at 10 mTorr and 100 W for frequencies of 3 and 14 MHz are shown in Fig. 9. (See Fig. 7 for EEDs at 6.78 MHz.) The EEDs at 3 MHz close to the coils and in the middle of the plasma are depleted at low energies due to the deeper penetration of rf fields into the plasma. Lorentz acceleration is also more important at the lower frequency, thereby helping to elevate the tail in the center of the reactor. These EEDs are well represented by bi-Maxwellian distributions. The EED close to the opposite wall, where the effect of collisionless heating is weak, has the lowest energy

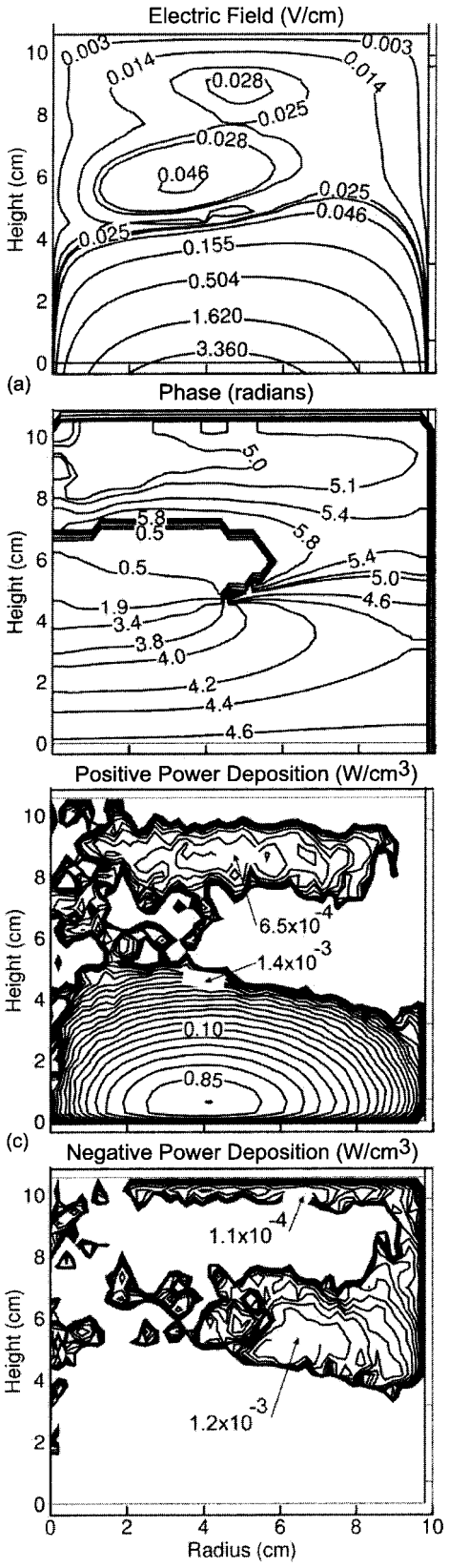


FIG. 11. Plasma properties at 10 mTorr, 200 W, 6.78 MHz. (a) The $\theta$ component of the electric field, (b) phase of the electric field, (c) positive power deposition to electrons, and (d) negative power deposition by electrons. Extrema in the electric field and power deposition occur at and beyond the edge of the classical skin depth.

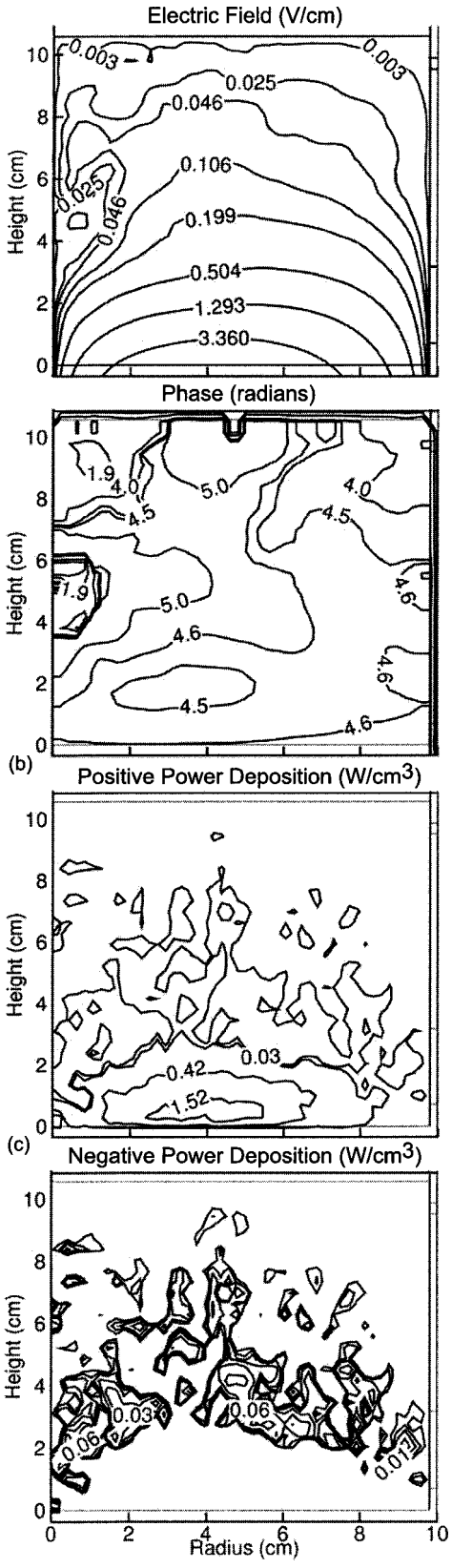


FIG. 12. Plasma properties at 10 mTorr, 200 W, 13.56 MHz. (a) The $\theta$ component of the electric field, (b) phase of the electric field, (c) positive power deposition to electrons, and (d) negative power deposition by electrons.

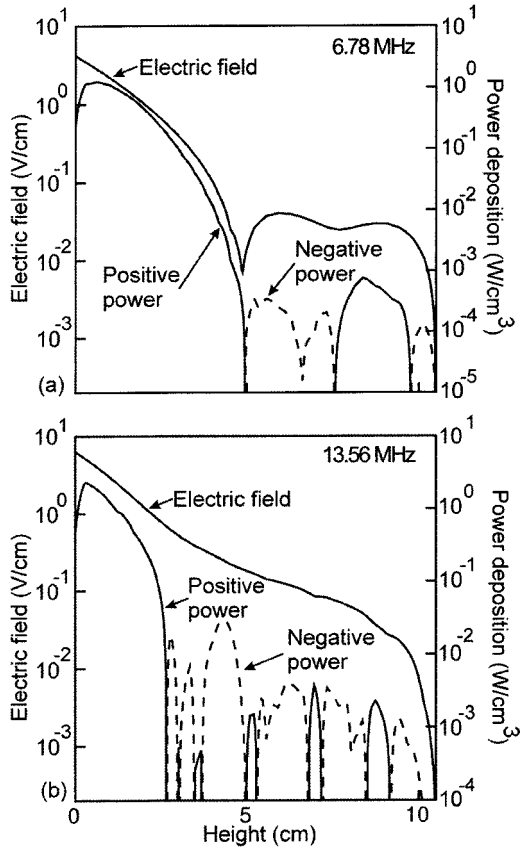


FIG. 13. The $\theta$ component of the electric field and power deposition at 100 W, 10 mTorr, $r=4.5$ cm for (a) 6.78 MHz and (b) 13.56 MHz. More layers of positive and negative power deposition are produced at the higher frequency.

tail. At 14 MHz, collisionless heating is important only close to the coils. The EED in this region is depleted at low energies whereas the EED in the middle of the plasma, where collisions dominate over stochastic heating, displays three-temperature distribution features. Close to the opposite wall, the EED at 14 MHz is rather similar to that at 3 MHz, being beyond the range of electrons heated in the skin layer at both frequencies.

The rf magnetic fields indirectly influence the electron kinetics by generating rf electric fields that directly transfer power to the electrons. The rf magnetic fields also directly affect the electron kinetics through the Lorentz force. Recently, it was suggested that this mechanism could significantly alter the form of EEDs in ICPs [9] and has been cited as the dominant acceleration method at low frequency and low pressures [7]. These conditions are usually met when the skin layer is anomalous. The EEDs calculated with and without the Lorentz force are shown in Fig. 10 for 1 mTorr, 100 W, and 3 MHz, conditions for which the skin layer is anomalous. When excluding the Lorentz force, the EED close to the coils is less depleted of low-energy electrons, indicating that the Lorentz force efficiently sweeps the skin layer of low-energy electrons.

In the middle of the reactor, the EED is peaked at very low energies when neglecting the Lorentz force. This is a consequence of electron pooling towards the center of the reactor to the peak in the electric potential. In contrast, the EED with the Lorentz force has a positive slope at very low energies and reaches a maximum at about 2 eV due to collisionless heating. The structure of the EED obtained with Lorentz force demonstrates that at low pressure and low frequency, when the skin layer is anomalous, the EEDs are strongly affected by noncollisional dynamics not only in the narrow region near the coils but also in the bulk plasma. The tail of the EED is correspondingly higher with the Lorentz force, a consequence of the long mean free path of the axially accelerated electrons. The effect of electron pooling will be overestimated if the Lorentz force is neglected. Close to the opposite wall, neglecting the Lorentz force underestimates the EED at low energies because too many electrons have pooled from this region towards the maximum in the plasma potential in the center of the reactor.

The EEDs obtained at higher pressures (>10 mTorr) and higher frequencies (>10 MHz), not shown here, are not significantly affected by the Lorentz force as the skin layer is at best only mildly anomalous. Such dependences of EEDs on pressure and excitation frequency, and the onset of anomalous behavior, are a consequence of collisionless electron heating. As such, the nonlocality parameter $\Lambda=(\lambda_{ef}/\delta_{ef})^2$, where $\lambda_{ef}$ is the distribution averaged electron mean free path and $\delta_{ef}$ is the characteristic penetration of the rf field penetration, characterizes the anomalous nature of the EED. $\lambda_{ef}$ decreases with pressure and $\delta_{ef}$ decreases with increasing frequency. When $\Lambda \ll 1$, the skin layer is normal, and the relation between the current density and the rf electric field is given by Ohm's law. When $\Lambda \geqslant 1$, the skin layer is anomalous and the acceleration of electrons in the skin layer affects EEDs over much of the reactor.

## IV. ANOMALOUS SKIN EFFECT AND NONLOCAL POWER DEPOSITION

The anomalous skin effect in ICPs [1,7–10,28,40] typically occurs for $\Lambda \geqslant 1$; low pressures, where the electron mean free path is comparable to or exceeds the classical skin depth and approaches the size of ICP reactor. While this phenomenon is widely accepted, different mechanisms have been suggested to explain it [1,9]. The first is based on the nonlocal conductivity due to the thermal electron motion. Power, transferred from the inductive rf electric field to electrons within a normal skin layer, can be transferred by thermal electron motion to the bulk plasma, and so produces an additional electric field. The second mechanism in part explains nonlocal behavior in ICPs by the Lorentz force resulting from the rf magnetic field. The spatial dependences of electric field and power deposition are discussed in this section to shed additional light on the topic.

The azimuthal component of the electric field $E_\theta$, phase $\varphi$, positive power deposition and negative power deposition for 200 W, 10 mTorr, and 6.78 MHz are shown in Fig. 11. $E_\theta$ and $\varphi$ monotonically decrease with distance from the antenna in the normal skin layer. Here power deposition is positive, which indicates that power is transferred from the electric field to the plasma. In the region above the normal skin layer, $E_\theta$ and $\varphi$ exhibit extrema and nodes, while the

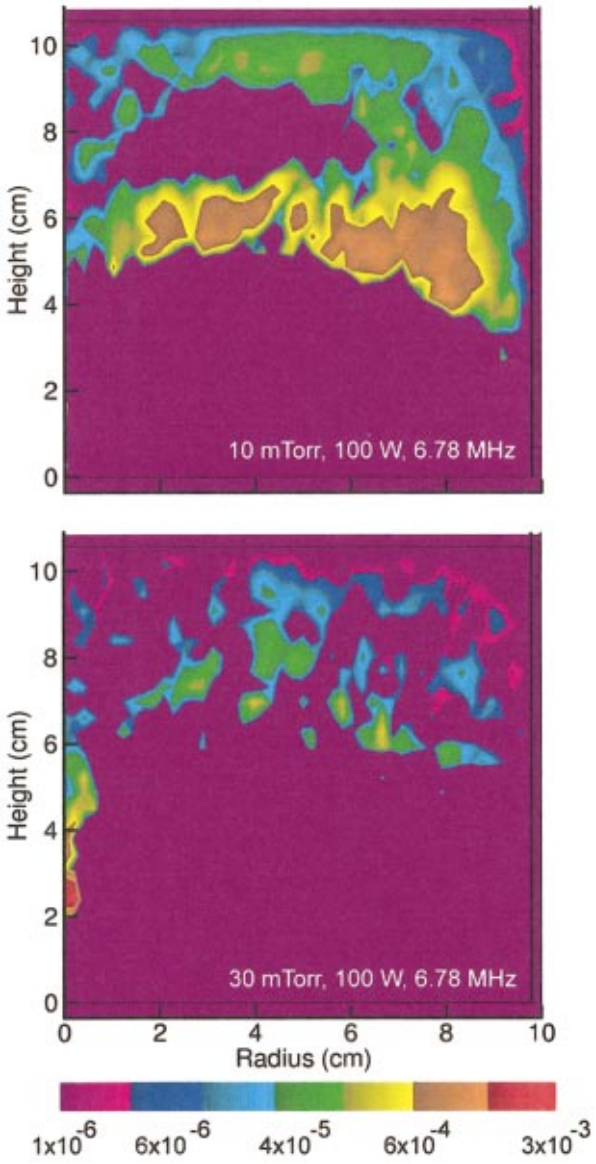


FIG. 14. (Color) Negative power deposition (W/cm$^3$) at 100 W, 6.78 MHz for (a) 10 mTorr and (b) 30 mTorr. Negative power deposition is more extended at the lower pressure.

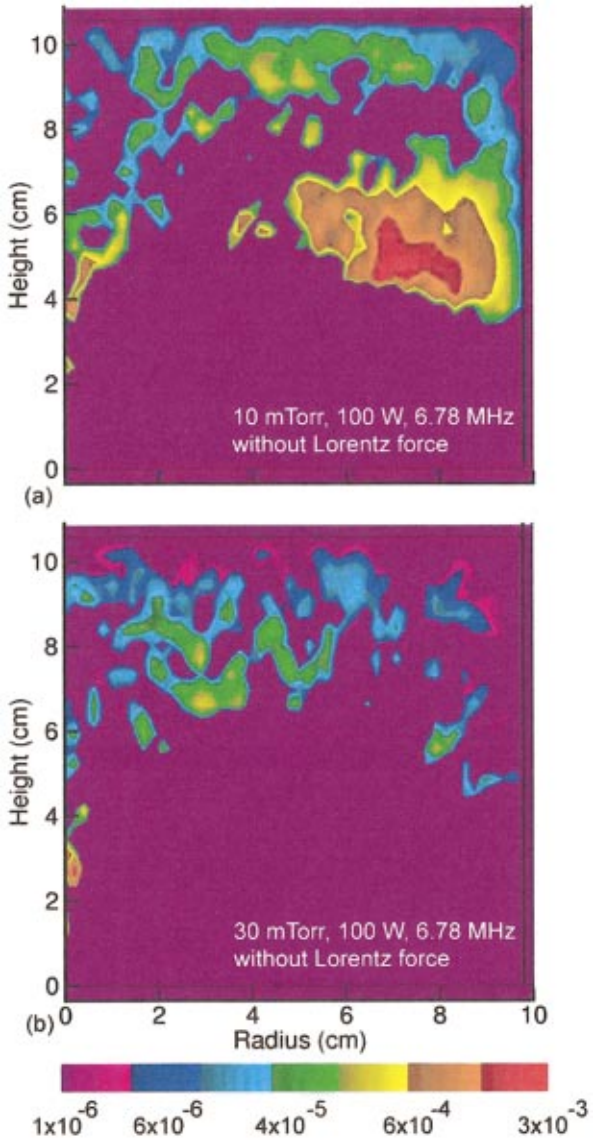


FIG. 15. (Color) Negative power deposition (W/cm$^3$) obtained while neglecting Lorentz force in EMCS at 100 W, 6.78 MHz. (a) 10 mTorr and (b) 30 mTorr.

power deposition alternates between positive and negative values resulting from noncollisional transport of electrons. This alternating of positive and negative power deposition, experimentally and theoretically obtained by Godyak and Kolobov [1] and recently calculated by Tyshetskiy, Smolyakov, and Godyak [41] is ultimately a consequence of electrons oscillating out of phase with the local electric field in such a manner that power transfer is to the field, as opposed to from the field. These electrons are initially accelerated in regions of larger electric field of more opportune phasing closer to the antenna. As a consequence, the maximum of negative power deposition occurs at the edge of the classical skin depth where electrons, reaching their maximum directed velocities, encounter an electric field of inappropriate phasing. This sequence of events can only occur if thermal motion of electrons is significant and mean free paths are commensurate with the thickness of the skin layer, so that electrons retain their directed momenta into regions of inappropriate phasing; that is, the skin layer is anomalous. Although nonmonotonically decaying electric fields are often observed for these conditions, we have found that negative power deposition also occurs with monotonically decaying electric fields, provided that the appropriate dephasing occurs. These trends are in agreement with the analytical predictions by Tyshetskiy, Smolyakov, and Godyak [41].

The electric field, phase, and power deposition for 13.56 MHz and 200 W (otherwise the same conditions as for 6.78 MHz) are shown in Fig. 12. $E_\theta$ contours are monotonic at midradius at the higher frequency, while the number of extrema and nodes for phase are substantially larger than at the lower frequency. $E_\theta$ is, however, nonmonotonic near the axis at 13.56 MHz. The increase in frequency also affects the positive and negative power deposition, as the alternation

between positive and negative power deposition is more frequent at the higher frequency. The maximum values of positive and negative power deposition increase as the shorter classical skin depth compresses the total power deposition into a smaller volume. The incidence of negative power deposition at 13.56 MHz occurs closer to the coils than it does for 6.78 MHz, owing to the decrease in skin depth with increase in frequency.

The electric field and power deposition at $r=4.5$ cm as a function of height are shown in Fig. 13 for 6.78 and 13.56 MHz. At 6.78 MHz, $E_\theta$ displays extrema that correspond to the border between regions of negative and positive power deposition. As the frequency increases, the skin depth decreases, whereas the magnitude of electric field and, correspondingly, the ability to deposit power within the normal skin depth increases. The number of negative power regions increases with the driving frequency. This dependence was experimentally found by Godyak and Kolobov [1]. The distance between the middle of the skin layer and the first zero crossing point of power deposition can be estimated by the multiplication of electron thermal velocity in $z$ direction, $v_z$, and the half of the rf field period, $z_0=v_z(2w)^{-1}$ [1,27]. Estimating $v_z=\frac{1}{3}\sqrt{2kT_e/m_e}$ at $T_e=3$ eV yields $3.4\times10^7$ cm/s. This gives $z_0=2.5$ cm at 6.78 MHz and $z_0=1.2$ cm at 13.56 MHz, which are in a good agreement with the results in Fig. 13.

Negative power deposition for 100 W and 6.78 MHz at pressures of 10 and 30 mTorr are shown in Fig. 14. The spatial distribution of negative power deposition is an indication of the collisionless nature of electron transport. The propensity for negative power deposition decreases with an increase in pressure in large part due to the decrease in mean free path that localizes the interaction between the electrons and electric field to the region at the boundary of the classical skin layer. Negative power deposition extends well beyond the classical skin layer at the lower pressure as mean free paths are commensurately longer.

The consequences of the Lorentz force due to the rf magnetic field on negative power deposition are shown in Fig. 15 for at the same conditions as in Fig. 14. By neglecting the rf magnetic field and the Lorentz force, we exclude this dominantly axial source of acceleration. As a result, electrons reside longer in the normal skin layer and are less likely to be accelerated into regions in which they are dephased with the electric field. As a result, the propensity for negative power deposition is less. This is particularly true at the edge of the classical skin layer.

## V. CONCLUDING REMARKS

To investigate electron transport in ICPs, a method for modeling $e$-$e$ collisions in Monte Carlo simulations was developed. In this method $e$-$e$ collisions are treated with a test particle approach using particle-mesh algorithms. The method was validated by comparing the calculated and measured electron densities, temperatures, and electron energy distributions in inductively coupled argon plasmas. The consequences of $e$-$e$ collisions on the formation of the low-energy portion of EEDs were discussed and we found that the increase in thermal conductivity afforded by the $e$-$e$ collisions reduces pooling of low-energy electrons near the peak in the plasma potential. It was also found that a decrease of power and an increase of pressure and/or frequency lead to a decrease in nonlocal behavior in ICPs. This result indicates that the anomalous skin effect occurs due to the noncollisional transport of thermal electrons. It was also observed that when the skin layer is anomalous, the Lorentz force significantly affects the EEDs by sweeping low-energy electrons out of the skin layer. Neglecting the Lorentz force overestimates negative power deposition.

## ACKNOWLEDGMENTS

This work was supported by CFD Research Corporation by subcontract on a small business innovative research phase II from the Defense Projects Research Administration, Sematech, the National Science Foundation (Grant No. CTS99-74962), Applied Materials, Inc., and the Semiconductor Research Corporation. The authors thank V. Kolobov, V. Godyak, and R. Piejak for their insight during this study.

[1] V. A. Godyak and V. I. Kolobov, Phys. Rev. Lett. **79**, 4589 (1997).
[2] R. Piejak, V. Godyak, and B. Alexandrovich, J. Appl. Phys. **81**, 3416 (1997).
[3] S. Rauf and M. J. Kushner, J. Appl. Phys. **81**, 5966 (1997).
[4] F. F. Dai and C.-H. Wu, IEEE Trans. Plasma Sci. **25**, 1373 (1997).
[5] V. A. Godyak and R. B. Piejak, J. Appl. Phys. **82**, 5944 (1997).
[6] V. A. Godyak, R. B. Piejak, B. M. Alexandrovich, and V. I. Kolobov, Phys. Plasmas **6**, 1804 (1999).
[7] V. A. Godyak, Bulg. J. Phys. **27**, 1 (2000).
[8] V. A. Godyak, B. M. Alexandrovich, and V. I. Kolobov, Phys. Rev. E **64**, 264061 (2001).
[9] J. D. Evans and F. F. Chen, Phys. Rev. Lett. **86**, 5502 (2001).
[10] G. Cunge, B. Crowley, D. Vender, and M. M. Turner, J. Appl. Phys. **89**, 3580 (2001).
[11] K. Nanbu, Phys. Rev. E **56**, 7314 (1997).
[12] V. Bobylev and K. Nanbu, Phys. Rev. E **61**, 4576 (2000).
[13] K. Nanbu, IEEE Trans. Plasma Sci. **28**, 971 (2000).
[14] K. Birdsall and A. B. Langdon, *Plasma Physics via Computer Simulation* (McGraw-Hill, New York, 1985).
[15] T. Makabe, in *Advances in Atomic, Molecular, and Optical Physics*, edited by M. Kimura and Y. Itikawa (Academic, San Diego, 2001), Vol. 44, pp. 127–154.
[16] V. I. Kolobov, D. P. Lymberopoulos, and D. J. Economou, Phys. Rev. E **55**, 3408 (1997).
[17] Y. Weng and M. J. Kushner, Phys. Rev. A **42**, 6192 (1990).
[18] R. Kinder and M. J. Kushner, J. Appl. Phys. **90**, 3699 (2001).
[19] M. Turner, Phys. Rev. Lett. **71**, 1844 (1993).
[20] V. A. Godyak, R. B. Piejak, and B. M. Alexandrovich, Plasma Sources Sci. Technol. **3**, 169 (1994).

[21] V. Vahedi, M. A. Lieberman, G. DiPeso, T. D. Rognlien, and D. Hewett, J. Appl. Phys. **78**, 1446 (1995).
[22] S. Rauf and M. J. Kushner, J. Appl. Phys. **81**, 5966 (1997).
[23] S. Lin and J. N. Bardsley, J. Chem. Phys. **66**, 435 (1977).
[24] M. Mitchner and C. H. Kruger, *Partially Ionized Gases* (Wiley, New York, 1973).
[25] M. A. Leiberman and A. J. Lichtenberg, *Principles of Plasma Discharges and Materials Processing* (Wiley, New York, 1994).
[26] G. A. Bird, *Molecular Gas Dynamics and the Direct Simulation of Gas Flows* (Oxford University Press, New York, 1994).
[27] V. A. Godyak, in *Electron Kinetics and Applications of Glow Discharges*, edited by U. Kortshagen and L. D. Tsendin (Plenum Press, New York, 1998), pp. 241–255.
[28] V. A. Godyak and V. J. Kolobov, Phys. Rev. Lett. **81**, 369 (1998).
[29] M. Hayashi, Nagoya Institute of Technology Report No. IPPJ-AM-19, 1991 (unpublished).
[30] K. Tachibana, Phys. Rev. A **34**, 1007 (1986).
[31] D. Rapp and P. Englander-Golden, J. Chem. Phys. **43**, 1464 (1965).
[32] R. H. McFarland and J. D. Kinney, Phys. Rev. **137**, A1058 (1965).
[33] P. Zapesochnyi and L. L. Shimon, Opt. Spectrosc. **11**, 155 (1966).
[34] L. Vriens, Phys. Lett. **8**, 260 (1964).
[35] A. N. Klucharev and V. Vujnovic, Phys. Rep. **185**, 55 (1990).
[36] H. W. Ellis, R. Y. Pai, E. W. McDaniel, E. A. Mason, and L. A. Viehland, At. Data Nucl. Data Tables **17**, 177 (1976).
[37] M. W. Kiehlbauch and D. B. Graves, J. Appl. Phys. **91**, 3539 (2002).
[38] V. Godyak, B. Piejak, R. Alexandrovich, and B. Smolyakov, Plasma Sources Sci. Technol. **10**, 459 (2001).
[39] U. Kortshagen, I. Pukropski, and M. Zethoff, J. Appl. Phys. **76**, 2048 (1994).
[40] K.-I. You and N. S. Yoon, Phys. Rev. E **59**, 7074 (1999).
[41] Yu. O. Tyshetskiy, A. I. Smolyakov, and V. A. Godyak, Plasma Sources Sci. Technol. **11**, 203 (2002).